Section 3

Computational studies including new techniques, the effect of varying model resolution, parallel processing

Dependency of horizontal and vertical resolutions, and turbulence schemes on snowfall forecasts

Teruyuki KATO

Japan Meteorological Agency/Meteorological Research Institute, Chiyoda-ku, Tokyo, Japan

1. Introduction

Kato and Hayashi (2007) showed that the Japan Meteorological Agency (JMA) nonhydrostatic model (Saito et al. 2007) with a horizontal resolution of 5 km overestimated snowfall over mountainous regions on the Japan-Sea side of the Japan Islands during winter monsoon season and underestimated it over plane regions, whereas such forecast tendencies are improved when a horizontal resolution of 1 km was used. In this study, the dependency of horizontal resolution (5km, 2km, 1km, 500m), the lowest height of vertical layers (LH: 20m, 10m), number of vertical layers (NV: 50, 70) and turbulence scheme (Mellor-Yamada level 3 (Nakanishi and Niino 2006): M-Y3, Deardroff (1980): DD) on snowfall forecasts is examined. The evaporation effect of hydrometeors is also investigated.

2. Experimental designs

At first, 12-hour forecasts are conducted every 6 hours during 16-20 December 2009 by the 5km-model whose initial and boundary conditions are produced from 6-hourly available JMA mesoscale analysis data with a horizontal resolution of 5 km. The model domain covers the area of 2500 x 2000 km^2 including the Sea of Japan (not shown). The other models (2km-, 1km- and 500m-models) are nested within forecasts of the 5km-model. These models have the same model domain (850 x 550 km^2) shown in Fig. 1, and their initial conditions are produced from 3-hour forecasts of the 5km-model. Figure 1 also shows the topography of the 1km-model. Model top is set about a height of 21 km in all models. Verification datasets for 5 days are produced from hourly output of the last 6-hour forecasts. A bulk-type microphysics parameterization scheme in which two moments are treated only for ice hydrometeors (i.e., snow, graupel and cloud ice) is used for precipitation processes in all models, and the Kain-Fritsch convection parameterization scheme is additionally used in the 5km-model. In the simulation with NV=70, so many vertical layers are set in the lower level that the 41^{st} vertical layer from the surface can have a depth of 100 m.

3. Results

The control simulation (LH: 20m, NV: 50, M-Y3) of the 1km-model well reproduces the horizontal distribution of five-day accumulated precipitation amounts observed raingauges (Fig. 2), although the amounts are slightly underestimated in the Hokuriku District. The precipitation amounts averaged over plain regions with a terrain height lower than 100m are about 90 mm both in the observation and the 1km-model control simulation (Fig. 3b), indicating that the 1km-model has also quantitatively high forecast accuracy.

Figure 3 shows the precipitation amounts of rain, snow, graupel and their total amounts, averaged over the sea and over plain regions with a terrain height lower than 100m in the domain left of black bold line in Fig. 1. The ratio of graupel precipitation amounts to total amounts of snow and graupel (i.e., snowfall) increases as the horizontal resolution becomes higher, and it exceeds 50 % around coastal regions in the 1km-model control simulation (Fig. 4). This high appearance frequency of graupel precipitation around coastal regions well agrees with observations. It should be noted that the 5km-model rarely simulates graupel precipitation, because it cannot represent strong updrafts that are necessary for the production of graupel due to a coarse resolution.

The difference between total precipitation amounts simulated by 1km-model (dx01) and 500m-model (dx005) with DD is small, whereas the 5km-model (dx05) considerably underestimates total amounts in both regions. In the simulations of DD = 10m (thin lines in Fig. 3), precipitation amounts for M-Y3 increase compared with that for DD independent of the horizontal resolution. This is because M-Y3 more largely transports upper-level strong winds to the near surface due to implicitly vertical mixing in comparison with DD, and consequently latent heat flux from the sea becomes larger (not shown).

The dependency of horizontal resolution, LH, NV and turbulence scheme on total precipitation amounts over the sea, plain regions (< 100 m), mountainous regions (> 500 m) and middle height regions (100 m ~ 500 m) are compared with the 1km-model control simulation (Fig. 5). The simulation with DD = 10m increases the amounts for all regions, while the other simulations increase the amounts over the sea and decrease them on land. The decrease of precipitation amounts on land is considerably small for NV=70 (L70) and the simulation in which evaporation rates of snow and graupel are set half (fac0.5). The results of fac0.5 could be brought from the suppression of organization of mesoscale convective systems (MCSs) due to the decrease of evaporation cooling over the sea, which decreases water vapor flux into the land. The precipitation amounts over the sea are considerably larger for DD than for M-Y3. This is because M-Y3 more forcibly produces convective mixing layer over the sea to reduce the atmospheric instability, and consequently MCSs more easily form and develop for DD than for M-Y3 to cause the increase of precipitation amounts.

References

Deardorff, J. W., 1980: Stratocumulus-capped mixed layers derived from a three-dimensional model. *Bound.-Layer Meteor.*, **18**, 495–527.

Kato, T. and S. Hayashi, 2007: Relation of Dec. 2005 heavy snowfall and cloud-top heights around the Japan-Sea side of the Japan Islands, estimated from objective analyses and forecasts of cloud-resolving model. *CAS/JSC Research Activities in Atmospheric and Oceanic Modeling*, **37**, 5.13-5.14.

Nakanishi, M. and H. Niino, 2006: An improved Mellor-Yamada level-3 model: Its numerical stability and application to a regional prediction of advection fog. *Bound.-Layer Meteor.*, **119**, 397-407.

Saito, K., J. Ishida, K. Aranami, T. Hara, T. Segawa, M. Nareta, and Y. Honda, 2007: Nonhydrostatic atmospheric models and operational development at JMA. *J. Meteor. Soc. Japan*, **85B**, 271-304.

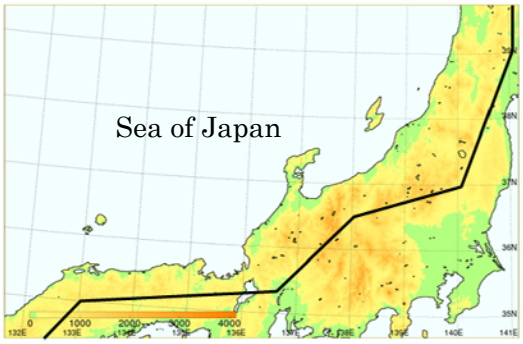

Fig. 1 Model domain and topography of the 1km-model.

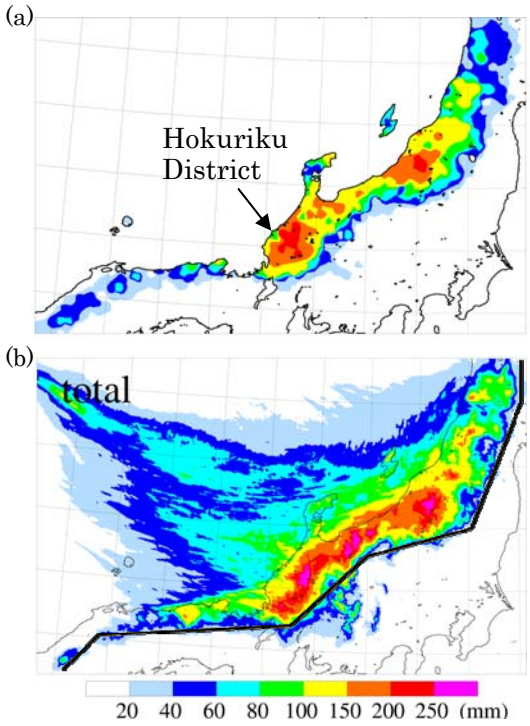

Fig. 2 Five-day accumulated precipitation amounts (a) observed by raingauges and (b) simulated by the 1km-model.

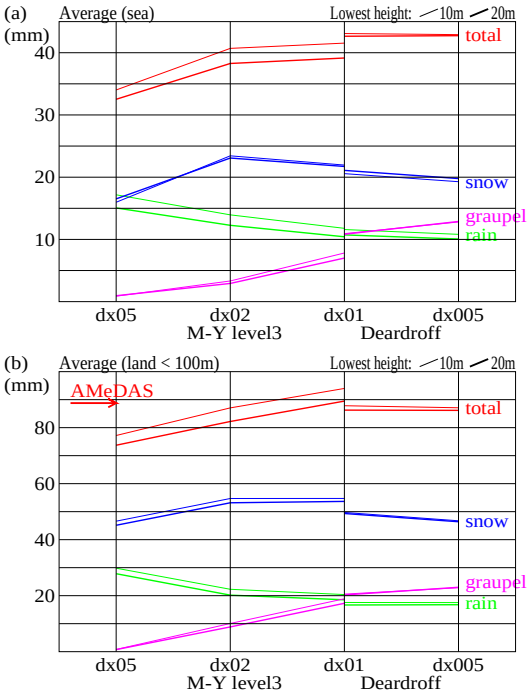

Fig. 3 Precipitation amounts averaged over (a) the sea and (b) the plain region with height lower than 100 m in the domain left of black bold line in Fig. 1. AMeDAS denotes the raingauge observation.

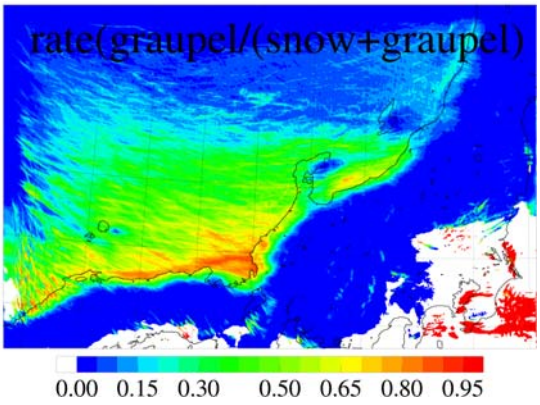

Fig. 4 Same as Fig. 2b, but for the ratio of graupel precipitation amounts to total amounts of snow and graupel.

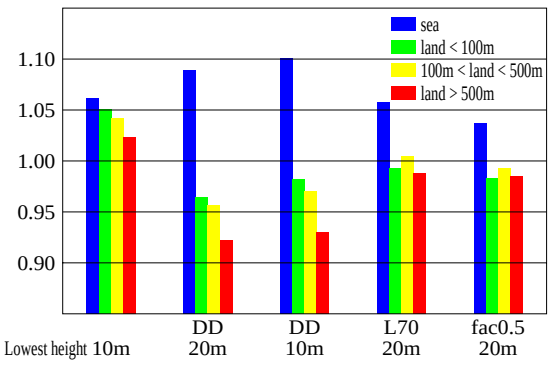

Fig. 5 Comparison with the control simulation of the 1km-model (LH: 20m, NV: 50, M-Y3). Axis of ordinate shows the ratios of averaged total precipitation amounts.

A statistical evaluation of typhoon structures simulated by JMA nonhydrostatic model

Wataru Mashiko
Meteorological Research Institute, JMA, 1-1 Nagamine, Tsukuba, Ibaraki 305-0052, Japan
(E-mail : wmashiko@mri-jma.go.jp)

1. Introduction

Significant progress has been made in track forecast of tropical cyclone (TC) mainly through the global numerical systems. However, intensity forecasting is still severely limited and one of the most challenging problems in TC forecast because inner-core processes of a few or tens of km horizontal dimension are essential for intensity change. To tackle this issue, a statistical evaluation of simulated typhoon structures, especially inner-core structures, was conducted using the regional nonhydrostatic model with high resolution.

2. Model description

The numerical model used in this study is the Japan Meteorological Agency Nonhydrostatic Model (JMA-NHM; Saito et al. 2006), which is operationally used in JMA. It is based on fully compressible equations with a map factor. While the physical parameterizations for precipitation, turbulence, microphysics, and radiation were unchanged from the JMA's operational run, the numerical diffusion and targeted moisture diffusion were slightly altered to reduce artificial mixing.

The model contains 955 x 757 grid points horizontally with grid spacing of 5 km, which covers a domain of 4770 x 3780 km. The model contains 58 levels with variable grid intervals from 40 m near the surface to 1048 m at the top. The initial and boundary conditions are provided from an operational global analysis of JMA that adopted a four-dimensional variational data assimilation system.

3. Experimental design

The experiments cover 13 significant typhoons which had less than 950 hPa of minimum sea-level pressure (MSLP) since 2008: 3 from the 2008 season, 8 from 2009, and 2 from 2010. The initial time is 12 UTC during the period from the genesis to mature stage, which contains 73 cases in total. The integration time is 120 hours. The model domain is optimally located using JMA best track data for each case.

4. Results

a. Track and intensity

At first, standard measures of the accuracy of the TC simulation, such as track and MSLP are described. While the model shows a good performance for typhoon track (Fig. 1a), large positive bias of MSLP exists especially at initial time (Fig. 1b). This is due to the initial condition provided by coarse-resolution global analysis. Large value of MSLP root mean square (~ 20 hPa) is found throughout the 120 h integration in spite of decreasing bias value. Figure 2a shows the comparison of MSLP between the simulation and the best track. The model cannot reproduce the MSLP of less than 920 hPa and tends to underpredict TC intensity. Rapid intensification such as less than – 1.75 hPa/hour of the MSLP tendency cannot also be reproduced.

b. Structures

The simulated MSLP against radius of maximum wind (RMW) is shown in Fig. 3a. The RMW of significant TCs with less than 940 hPa MSLP, which has generally axisymmetric inner-core structure, ranges from 40 to 80 km. It is quite large compared to the estimation from satellite

microwave imagery. Figure 3b illustrates the secondary circulation of major Typhoon LUPIT (2009) with MSLP of 930 hPa. Radial inflow layer is about 1.8 km depth peaking near the surface, and outflow is significant around at a height of 16 km. They are higher than the general structure of TCs. Further investigations as to resolution dependence and physical parameterizations will be needed to evaluate the performance of JMANHM and improve the TC intensity forecast.

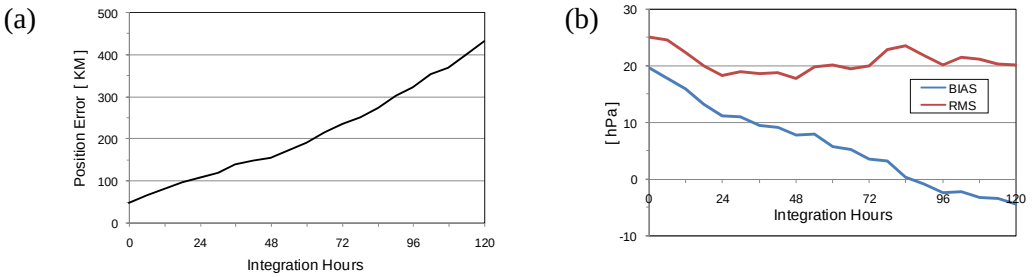

Fig. 1. (a) Average position error and (b) intensity error of bias (blue line) and root mean square (red line) for JAMNHM.

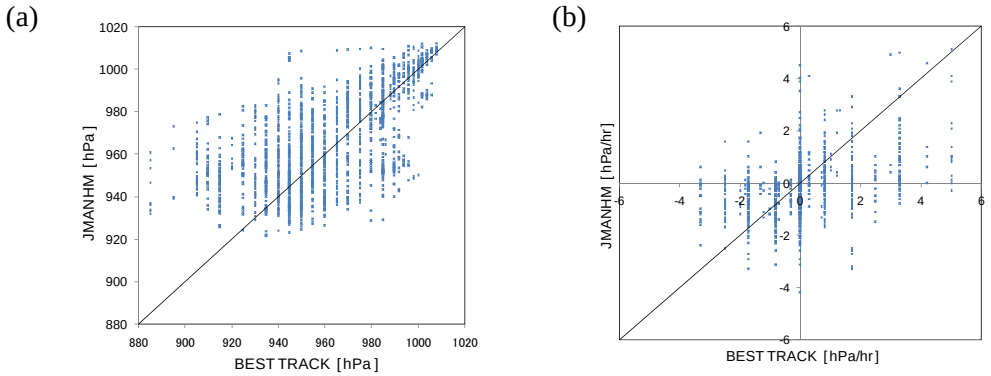

Fig. 2. Comparison of (a) minimum sea-level pressure (MSLP) and (b) its tendency between JMANHM and best track data.

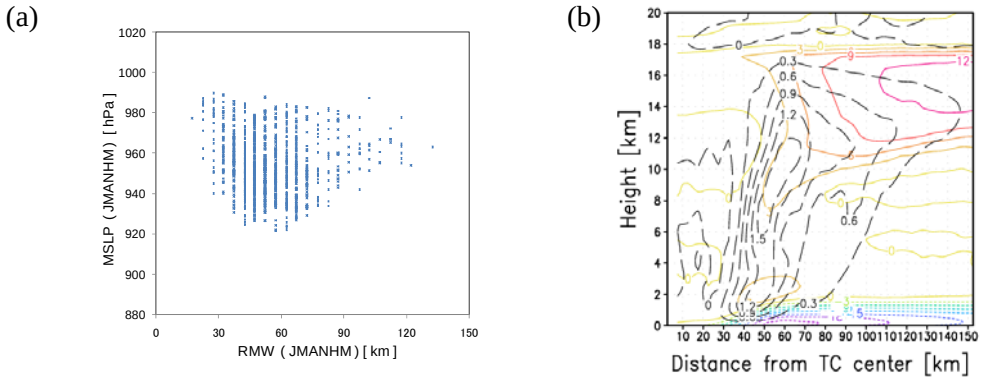

Fig. 3. (a) Minimum sea-level pressure (MSLP) against radius of maximum wind (RMW) simulated by JMANHM. (b) Radius-height plot of azimuthally averaged vertical motion (black broken lines) and radial wind (color contours) for Typhoon LUPIT (2009).

REFERENCES

Saito, K., T. Fujita, Y. Yamada, J. Ishida, Y. Kumagai, K. Aranami, S. Ohmori, R. Nagasawa, S. Kumagai, C. Muroi, T. Kato, H.Eito, and Y. Yamazaki, 2006: The operational JMA nonhydrostatic mesoscale model. Mon. Wea. Rev., 134, 1266-1298.

Dependence on resolution of the development of shallow cumulus over land

Masaomi Nakamura *
*Meteorological Research Insititute, Tsukuba, Ibaraki, 305-0052, JAPAN
manakamu@mri-jma.go.jp

1. Introduction

Recent computational resources enable meso-scale simulation with fine resolution by directly representing deep cumulus convection. However, these models are still insufficient in resolution to represent shallow cumulus. Then, as a practical matter, it is interesting to see how shallow cumulus is represented in these models and how the result is affected by an insufficiency of resolution. In this report the dependence on the grid spacing of the development of fine day's shallow cumulus over land are studied with Japan Meteorological Agency (JMA) nonhydrostatic model (hereafter referred to as NHM), based on an idealized setting for LES simulation intercomparison experiment of GCSS ARM case (Brown, 2002), which is built on observations made in the Southern Great Plains on 21 June 1997.

2. Experimental settings

Horizontally uniform surface sensible- and latent-heat fluxes with diurnal variation are prescribed (Fig.1). A large-scale horizontal pressure gradient is applied, which is equivalent to a geostrophic wind of 10m/s in the x direction at latitude 36N. Large-scale potential-temperature and moisture tendencies are imposed, which are small and do not essentially affect the results. The boundary conditions are periodic in the x and y directions. To initiate atmospheric motions, very small perturbations are applied in the initial filed.

Experiments are executed for grid spacing 67m (standard experiment in Brown et al., 2002), 250m, 500m, 1km with Deardorff's turbulence scheme and 2km with Mellor Yamada scheme modified by Nakanishi and Niino (MYNN scheme), represented as M67, M250, M500, M1k and M2kMY, respectively. All the models have horizontal grids of 100x100. The vertical resolution is 40m from the surface to about 5000m for M67 and stretched from 40m near the surface to about 900m at the top for other models. The models are run for 14 hours.

2. Results

It is not shown, but M67 shows results similar to those of LES models described in Brown et al. (2002). Figure 2 shows that grid-scale motions to transport heat from the surface to upwards start at around t=3, 4, and 6 hr for M250, M500 and M1k, respectively. These times are nearly equal to the time when the mixed layer has developed roughly to a depth of the model horizontal grid spacing. Before these times, the sub-grid scale turbulence transports heat in the mixed layer. The development of cloud layer above the mixed layer is also delayed for models with coarser resolution. M67's result is similar to that of M250, though grid-scale motions starts a little (about 30 minute) earlier in M67 than M250.

It is seen from Fig.3 that domain averaged vertical distributions of water vapor mixing ratio are not different so much between the models. It is true for potential temperature. (not shown). However, M2kMY has too-low cloud top and problematic distribution in the cloud layer (700m-2200m). Fig. 4 shows that M1k gives a little larger cloud amount than other models at levels near cloud top. M2kMY have no grid-scale cloud water, but sub-grid scale cloud amount is diagonized. The development to improve the problem caused by the current MYNN scheme, as seen in M2kMY, is now undertaken at JMA.

The horizontal cross sections of moisture field at an altitude of 2000m are presented in Fig.5 for M67, M250 and M1k. Note that the absolute scales are different; the domain sizes are 6.7kmx6.7km and 25kmx25km and 100kmx100km for M67. M250 and M1k, respectively. The diameters of active transporting clouds are about 0.2-0.6km in M67 , 0.5-1.2km in M250 and 2-4km in M1k. The cloud sizes are very different between the models, though the domain-averaged quantities are similar (Figures 3 and 4). It seems that grid-scale motions of the models are regulated in average by the requirement to transport heat from the

surface to the free atmosphere, which may lead to a similar cloud amount and domain-average vertical profiles, if the model has a grid spacing finer than about 1km, which is nearly equal to the maximum vertical extent of the mixed layer.

3. Summary and concluding remarks

The switching of a roll to transport heat vertically from sub-grid to grid scale occurs at different times depending on the model resolution. It occurs earlier for higher resolution models: roughly speaking, it occurs when the vertical scale of mixing reaches model's horizontal grid spacing. The clouds represented are very different between the models, but, when once grid-scale motions develop, the domain-averaged quantities such as cloud amount and vertical profiles do not differ so much between the models, at least for resolution finer than ～1km. It should be kept in mind that these results are based on one special case and various case studies are needed.

4. References

Brown, A. R., et al., 2002: Large-eddy simulation of the diurnal cycle of shallow cumulus convection over land. *Q. J. R. Meteorol. Soc.*, **128**, 1075-1093.

Saito, K., J. Ishida, K. Aranami, T. Hara, T. Segawa, M. Narita, and Y. Honda, 2007: Nonhydrostatic atmospheric models and operational development at JMA. *J. Meteor. Soc. Japan*, **85**, 271-304.

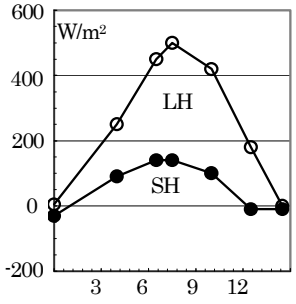

Figure 1. Time evolution of sensible (SH) and latent heat (LH) fluxes from the surface specified in the experiments.

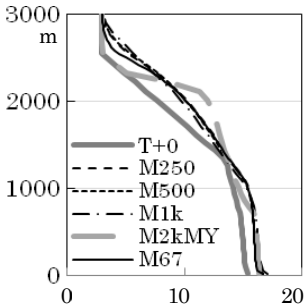

Figure 3. Vertical profile of water vapor mixing ratio (g/kg) averaged over the domain at t=10hr.

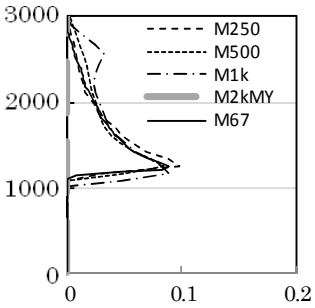

Figure 4. Vertical distribution of cloud amount at t=10hr.

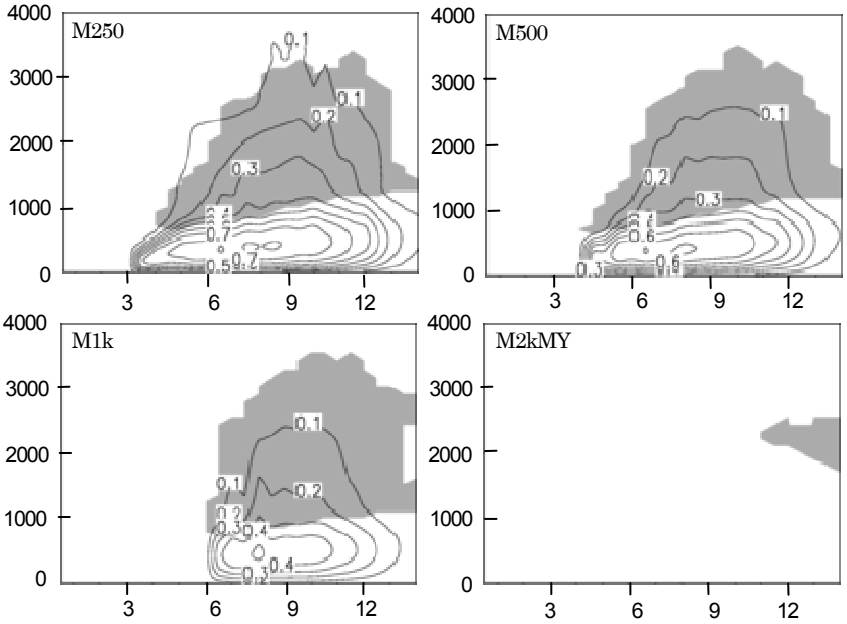

Figure 2. Time-height section of the domain-averaged square root of vertical velocity, w (contour). Shaded region represents cloud region.

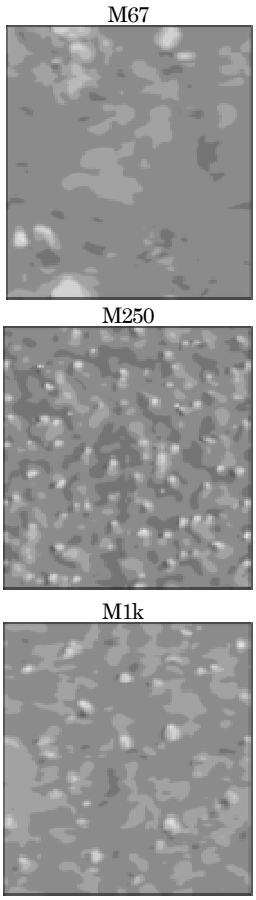

Figure 5. Horizontal distribution of water vapor mixing ratio at 2000m at t=10hr.

Tropical cyclone track forecasts using a limited-area model: sensitivity to the lateral boundary conditions

Matthieu Plu[1] and Ghislain Faure
Météo-France, Laboratoire de l'Atmosphère et des Cyclones,
Unité Mixte CNRS – Météo-France – Université de La Réunion
[1]: corresponding author, e-mail: matthieu.plu@meteo.fr

Abstract: The link between tropical cyclone track forecasts by Aladin-Réunion limited-area model and by its coupling model Arpege is investigated in the South-West Indian Ocean. A significant impact of the coupling model on the LAM track forecasts is shown after the 2-days term, although the sensitivity to initial conditions remains predominant in some cases.

1. Introduction

Limited-area models (LAM) at high resolution are commonly used for tropical cyclone (TC) forecasting. In the South-West Indian Ocean, Météo-France operates the LAM Aladin-Réunion (Montroty et al, 2008) at 8 km horizontal resolution over the domain [31.5E,88.5E] × [0,32S]. Aladin has its own 3D-Var assimilation cycle and it assimilates wind bogus pseudo-observations to initialize TCs. Its lateral boundary conditions come from the Arpege coupling global model (CGM), at a 3-hour coupling frequency. Both models have the same dynamics and physics.

On average, the cyclone track forecasts by Aladin are better than the ones by Arpege until the final term (84 h). Little is known about the sensitivity of track error to the CGM, and what skill change may be expected from using a different CGM. To address this question, two diagnostics are presented here: a correlation analysis between errors by different models and some case studies.

2. Statistical link between track error in a LAM and in its coupling global model

The TCs of all intensities during the 2009-2010 season (from october 2009 to april 2010) are considered here. Correlations are computed between the forecast errors by different models (Fig. 1): Aladin, Arpege and the European Centre for Medium-Range Weather Forecasts operational deterministic model (IFS).

The correlation between the independent models (Arpege vs IFS, Aladin vs IFS) is around 0.5 at the initial forecast time, but then it vanishes steadily until it reaches a zero value at 84 h. The correlation between Aladin and its CGM Arpege conversely starts at a low correlation value (around 0.2), increases rapidly until 24 h and then increases steadily until it reaches the 0.6 value at 84 h. The low correlation at 0 h lead time may be due to the assimilation of wind pseudo-observations in the Aladin 3D-Var, which has a strong impact on the TC position in the analysis. The correlation between the LAM and its CGM reaches high values compared to the independent models after 48 h. But track errors of the LAM and of its CGM are not perfectly correlated, even at 84 h: the LAM forecast tracks are partially independent of the CGM forecast tracks.

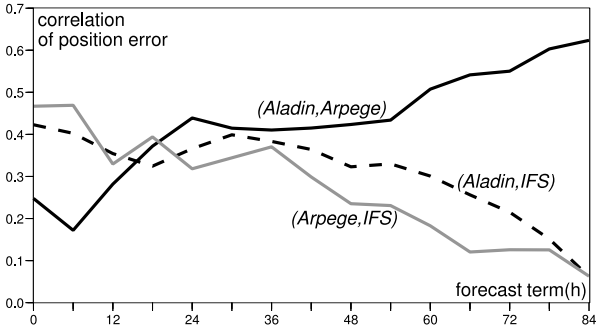

FIG. 1. Evolution with the forecast lead time of the correlation between the position errors of the TC forecasts by Aladin, its CGM Arpege and IFS, during the 2009-2010 cyclone season.

3. Sensitivity of track error in the LAM to its coupling model

The sensitivity of TC track forecasts by the LAM to its CGM is investigated on two TCs, Gael (February 2009) and Edzani (January

2010), which have both reached an intense stage (maximum winds over 90 kts). Two configurations of the stretched CGM Arpege have been run, one at the truncation T538C2.4 (roughly 55 km equivalent grid spacing), called ArpT538, and the other one at T798C2.4 (roughly 35 km equivalent grid spacing), called ArpT798. The Aladin assimilation cycles and forecasts coupled with both configurations of Arpege have also been run, leading to the associated forecasts called AlaT538 and AlaT798. In both experiments, the LAM configurations are the same. The initial instants of the forecasts are at 00 UTC and at 12 UTC. The mean evolution of the position error along the forecast terms for these 4 models on several forecasts (Fig. 2) reflects the sensitivity of the LAM to its CGM.

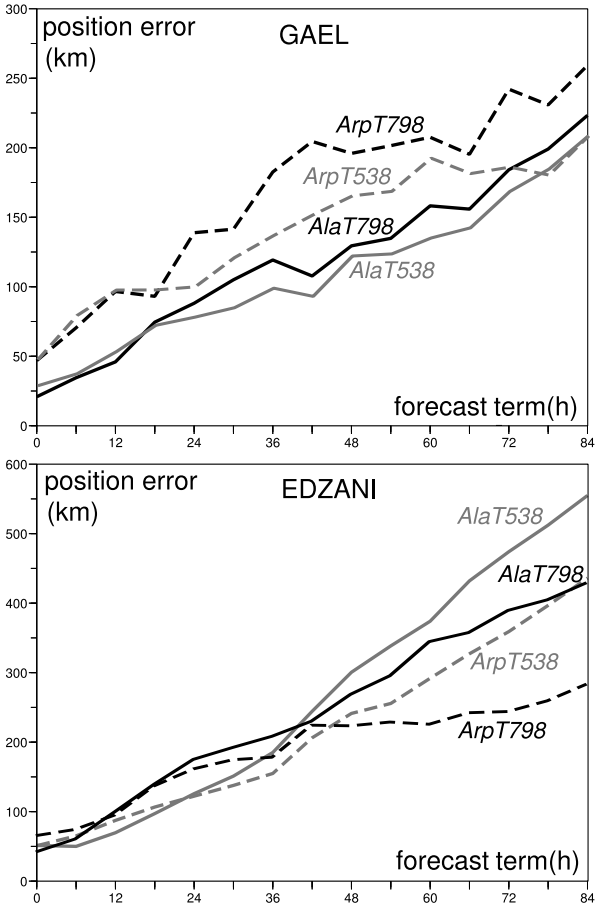

FIG. 2. Evolution for the TCs Gael (top) and Edzani (bottom) of the error of the forecast positions by the CGM Arpege at truncation T538C2.4 (ArpT538, dashed grey), at truncation T798C2.4 (ArpT798, dashed black) and by the associated LAM Aladin (AlaT538, solid grey) and (AlaT798, solid black). The curves are an average of 7 forecasts for Gael and 9 forecasts for Edzani.

Gael and Edzani illustrate two different configurations of position errors. In the case of Gael, the LAM performs better than its CGM, which happens the most frequently. For Edzani, the CGM performs globally better than the LAM. In both cases, the error reduction at long terms (after 48 h) between ArpT538 and ArpT798 apply partially to the LAM forecasts. Moreover, in the case of Edzani, ArpT798 is the only model that is able to represent an abrupt change of track: even AlaT798 does not show it. In such a case, the initial conditions in the LAM may play a critical role.

4. Conclusion

This short study documents how changing the CGM used for the lateral boundary conditions of the LAM Aladin may change its performance for TC track forecasts. At short range (below 48 h terms), the forecast position error of the LAM is not much linked to the CGM error. After 48 h, the CGM performance has an impact on the LAM, and it explains about an half of the LAM forecast error. Still, in some cases, the LAM track forecast is only slightly linked to the CGM one, which suggests that sensitivity to the initial conditions is predominant.

These results, which may depend on the size of the domain, are consistent with some previous studies using a different model in Taiwan (Hsiao et al, 2009). Better data assimilation in LAM for tropical cyclones is critical for improving track forecasts, but the performance of coupling global model also deserves attention.

References

Montroty, R., F. Rabier, S. Westrelin, G. Faure and N. Viltard, 2008: Impact of wind bogus and cloud and rain affected SSM/I data on tropical cyclones analyses and forecasts. *Q. J. R. Meteorol. Soc.*, 134, 1673–1699.

Hsiao, L.-F., M. S. Peng, D.-S. Chen, K.-N. Huang and T.-C. Yeh, 2009: Sensitivity of typhoon track predictions in a regional prediction system to initial and lateral boundary conditions, *J. Appl. Meteor. Clim.*, 48, 1913–1928.

Thanks Room is missing to thank all the colleagues in Météo-France Toulouse with whom we collaborate to develop LAM for tropical cyclone forecasting in the South-West Indian Ocean!

Development of a Global Grid Model for Hyper-Parallel Computing in JMA

Masami Sakamoto, Chiashi Muroi, Junichi Ishida
Numerical Prediction Division, Japan Meteorological Agency
1-3-4 Otemachi, Chiyoda-ku, Tokyo 100-8122, Japan
(e-mail: masami.sakamoto-a@met.kishou.go.jp)

1. Introduction

Computational efficiency in hyper-parallel computing environments is important for the future operation of a higher-resolution NWP model. Japan Meteorological Agency (JMA) started development of a global grid model in 2009. Since the global spectral model JMA currently uses requires global communication among computational nodes, feasibility of global grid models has been examined. The shallow-water test using the Yin-Yang grid configuration proposed by Kageyama and Sato (2004) are presented here.

2. Discretization method and grid configuration

The finite volume method (FVM) is used because of its advantages not only in computational efficiency for parallel computing but also in the conservation of mass. The flux calculation method adopted in this study is very similar to the one developed for ASUCA (Ishida et al. 2010) in which the up-wind method with a flux limiter proposed by Koren (1993) is used. With this scheme, global communication among nodes is unnecessary except for treatment of the output. The third-order Runge-Kutta scheme of ASUCA is also used as the time integration method.

As for the global grid configuration, the Yin-Yang grid shown in Figure 1 (a) is used. To prevent instability around the grid system border, the over-set length is set to be more than three grid points according the results of Baba et al. (2010). This configuration does not force the use of numerical diffusion or viscosity to stabilize time integration even with grid sizes of less than 1 degree. For parallel computation among distributed memories, the two-dimensional domain decomposition method is used. Figure 1 (b) shows the distributions of domains in the latitude-longitude projection covered by each calculation node when 8, 16, and 32 calculation nodes are used. The size of the area including the overset region for each grid is the same, and communication partners are easy to find using the coordinate transformation by Kageyama and Sato (2004).

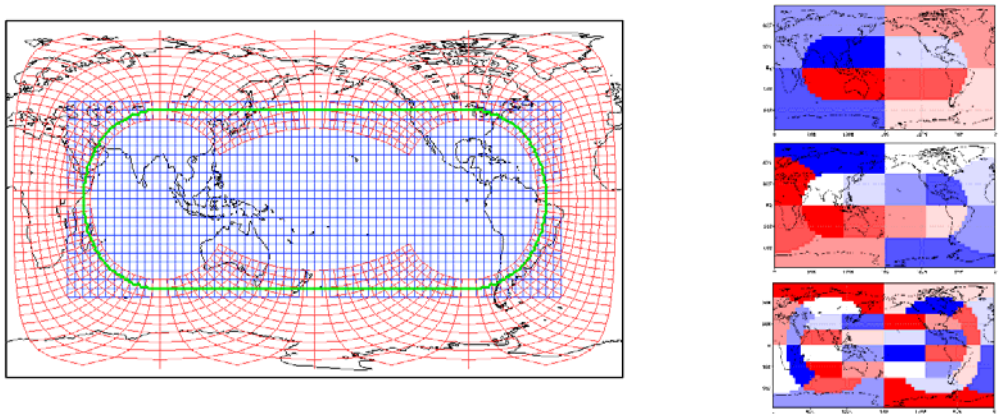

Figure 1. Configuration of the Yin-Yang grid in the lat.-long. map projection (a: left panel) and the domains covered by individual calculation nodes in two-dimensional domain decomposition (b: right panel). In panel (a), the bold green line indicates the yin-yang grid system borderline; the blue cells belong to the Yin grid, and the red ones are for the Yang grid. In (b), the domains are shown for cases in which 8 (top), 16 (middle), and 32 (bottom) calculation nodes are used.

3. Shallow water test

The zonal geostrophic flow test proposed by Williamson et al. (1992) was examined under various resolutions and with the different numbers of nodes used in the calculations. Figure 2 shows the results of five-day forecasts when α (the inclination angle of speed) is equal to zero. As shown in the figures, the level of error remains quite small. Figure 3 shows time series of the standard norms proposed by Williamson et al. (1992). The results indicate a reasonable level of accuracy in relation to those of other shallow water studies.

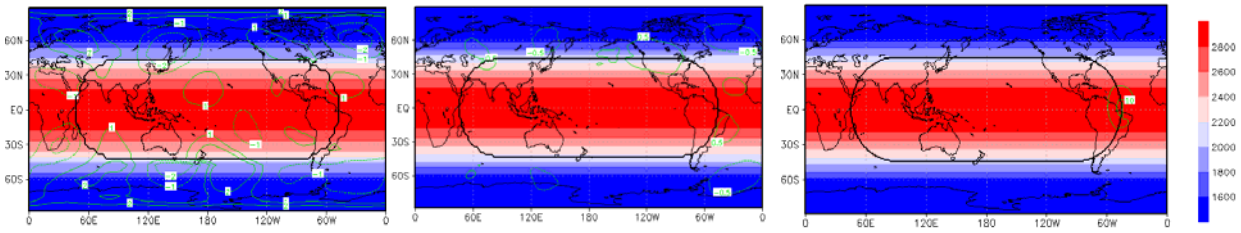

Figure 2. Results of five-day forecast for the zonal geostrophic flow test with spatial resolutions of 4.5 degrees (left: a), 2.25 degrees (center: b) and 1.125 degrees (right: c). The shading indicates the free surface height (m), and the green contours represent the level of error (m) from the theoretical truth. The time-step lengths are (a) 10 min., (b) 3 min. and (c) 1 min.

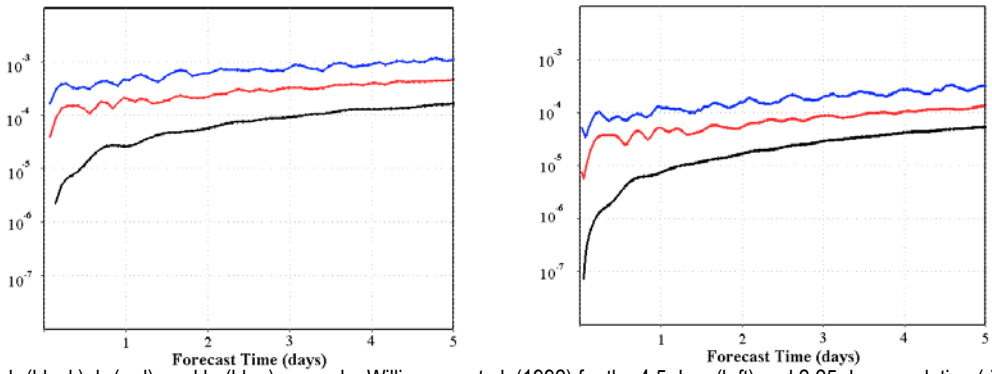

Figure 3. The l_1 (black), l_2 (red), and l_∞ (blue) norms by Williamson et al. (1992) for the 4.5 deg. (left) and 2.25 deg. resolution (right)

4. Summary

Zonal geostrophic flow test was performed using the FVM and the Yin-Yang grid. The discretization method and the grid configuration demonstrated effectiveness in the development of a global grid model for hyper-parallel computing. So far, shallow water test results have been successful even without the use of numerical diffusion or viscosity.

References

Baba, Y., K. Takahashi, T. Sugimura, and K. Goto 2010: Dynamical Core of an Atmospheric General Circulation Model on a Yin-Yang Grid. Monthly Weather Rev., 138, 3988 – 4005.

Ishida, J., C. Muroi, K. Kawano, Y. Kitamura 2010: Development of a New Nonhydrostatic Model ASUCA at JMA. CAS/JSC WGNE Research Activities in Atmospheric and Oceanic Modeling.

Kageyama, A. and T. Sato 2004: "Yin-Yang Grid": An Overset Grid in Spherical Geometry. Geochem. Geophys. Geosyst. 5, Q09005, doi: 10.1029/204GC007.

Koren, B., 1993: A robust upwind discretisation method for advection, diffusion and source terms. Numerical Methods for Advection-Diffusion Problems, Vieweg, Braunschweig, 117.

Williamson, D. L., J. B. Drake, J. J. Hack, R. Jakob, and P. N. Swarztrauber 1992: A Standard Test Set for Numerical Approximations to the Shallow Water Equations in Spherical Geometry. J. Comp. Phys. 102, 211 – 224.

A FORMAL APPROACH FOR SMOOTHING ON VARIABLE-RESOLUTION GRID
Part I: Design and application for Cartesian coordinates

Dorina Surcel and René Laprise
ESCER, Université du Québec à Montréal, Montréal, Québec, Canada (colan@sca.uqam.ca)

Global climate models with variable resolution are used to improve the representation of regional scales over an area of interest, avoiding the nesting issues of the limited-area models and reducing the computational costs compared to global uniform high-resolution models. To address some potential problems associated with the stretching and anisotropy of the computational grid, a general convolution filter operator was developed. The main feature of this filter is to locally remove scales shorter than a user-prescribed spatially varying length scale.

Over non-uniform grids, the only scales that can be represented over the entire domain are those with length scales larger than or equal to twice the maximum grid spacing $\Delta x_{\max}$. In a stretched-grid model, it would be possible to remove anisotropic features associated with fine-scale structure of the mesh in only one dimension, such as in the arms-of-the-cross region surrounding the high-resolution area of interest. This may be an effective means of controlling aliasing of fine-scale features while they exit the high-resolution region and enter in the low-resolution part of the domain. In this case, the numerical filtering operator could suitably remove the unwanted small scales outside the uniform high-resolution area.

The convolution operator was chosen to design the filtering formula. For a signal ψ, the filtered value $\overline{\psi}$ is: $\overline{\psi}(x) = (\psi * w)(x) = \int_{-\infty}^{\infty} \psi(x) \cdot w(x-s)\,ds$. Using the convolution theorem and taking the Fourier transform of the initial ψ and the filtered $\overline{\psi}$ fields to evaluate the ratio of their spectral amplitudes, one finds that the required weighting function w is the inverse Fourier transform of the desired response function (e.g. Surcel 2005). The numerical filtering operator that will remove all the waves that are not correctly represented outside the high-resolution region has a spectral response that corresponds to keeping unchanged the large scales with wavenumber smaller than $a = 2\pi/2\Delta x_{\max}$ (corresponding to wavelengths larger than $2\Delta x_{\max}$ that are resolved everywhere on the grid), and removing entirely small scales with wavenumber larger than a chosen value of $b \le 2\pi/2\Delta x_{\min}$, with a gradual transition in between to reduce Gibbs' phenomenon. The convolution theorem then gives $w(d) = \frac{\pi}{2} \cdot \frac{\sin ad + \sin bd}{d} \cdot \frac{1}{\pi^2 - d^2(b-a)^2}$, where $d = x - s$. Although the formal definition of the convolution exists for continuous space, its practical application needs a definition using a discrete set of points. Also, the presence of non-vanishing values over the entire domain is problematic because of excessive computational costs. Given that the values become small after some distance from the origin, truncating the weighting function after some distance can result in an important reduction in computational costs. While the truncation distance is an important parameter for the precision of the filter, the distance between the wavenumbers *a* and *b* affects also the choice of the truncation distance and subsequently the precision of the filter. A weighting function corresponding to an abrupt change in the spectral response contains large oscillations, and needs a large truncation distance, while a more gradually varying response function gives rise to a narrow weighting function, and thus to a much smaller acceptable truncation distance, in order to approximate adequately the theoretical response.

The application of the convolution filter for a variable resolution domain is tested considering a periodic 1D stretched grid $[0, 2\pi]$ with a stretching factor $S = \Delta x_{\max}/\Delta x_{\min} \cong 4$. This grid contains 60 to 64% from the total number of grid points in the high-resolution area, even if the area represents only 1/3 from the entire domain. The filter is tested using the 1D test-function as $\psi(x) = \psi_l(x) + \psi_n(x)$, where ψ_l is a large-scale wave representing the physical signal that is properly represented on the entire domain, and ψ_n is a small-scale wave representing the noise which is chosen to be zero in the low-resolution part of the domain, gradually increased in the stretching areas, and is maximum in the high-resolution area of the domain. The skill of the filter is quantitatively evaluated by comparing the filtered solution $\overline{\psi}$ with the expected analytical

solution ψ_l, using two scores: the normalized root-mean square error (*NRMS*) that is computed between the filtered solution and the expected analytical solution, and the normalized conservation ratio (*NCR)* calculated as the mean error between the filtered and unfiltered solution (Surcel and Laprise, 2010).

A first example presents a test function containing a noise with wavenumber $k_n = 2\pi/4\Delta x_{\min}$. The convolution filter used a weighting function w_1 defined by $a = 2\pi/2\Delta x_{\max}$ and $b = 1.5a$; in this case a truncation distance $d_{\max} = 5\Delta x_{\max}$ was adequate to completely remove the noise while maintaining the large-scale signal. The effects of using different weighting functions was studied employing the same test function and two different weighting functions: w_1 ($a = 2\pi/2\Delta x_{\max}$; $b = 1.5a$) and w_2 ($a = 2\pi/2\Delta x_{\max}$; $b = 2a$). The *NRMS* score (Fig. 1b) shows that the noise is completely removed if an adequate truncation distance is used and this distance is shorter for the filter with a more gradual response (w_2). In this case we note also a better conservation expressed by a *NCR* score, which approaches zero for a truncation distance larger than $10\Delta x_{\min}$ as it can be seen in Fig. 1c.

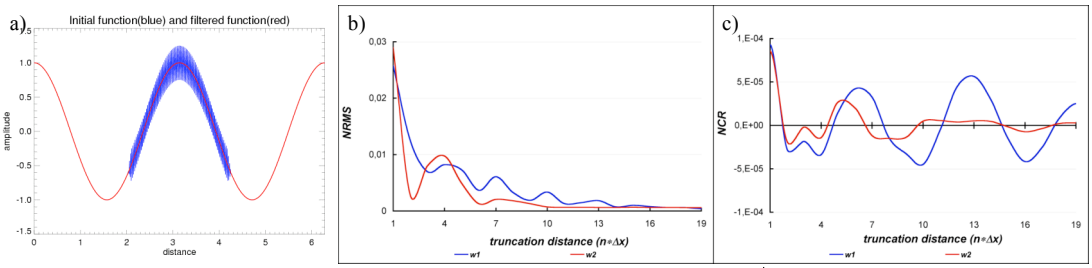

Figure 1. (a) The initial test function (blue) containing a noise with wavenumber $k_n = 2\pi/4\Delta x_{\min}$ and the filtered field (red) are represented on a grid with $S \cong 4$. The convolution uses the weighting function w_1 and a truncation distance $d_{\max} = 5\Delta x_{\max}$. The *NRMS* (b) and the *NCR* (c) scores as a function of the truncation distance, for two different weighting functions.

The formal approach developed in 1D is generalized for two-dimensional domains. The 2D convolution uses a weighting function that is the product of two 1D functions, similar with those used in one-dimensional case. In practice, the 2D filtered function is obtained conveniently by successive applications of 1D filter in each direction. It is important to reiterate that in our proposed convolution filter approach, the weights are calculated using physical distances rather than grid-point indices.

Similarly to our tests in 1D, test functions using 2D sinusoidal waveforms were chosen to represent the large-scale signal that will be retained by the filter and the noise that will be removed. The example presented in Fig. 2 shows the initial signal (a) and the filtered function when the convolution uses the weighting function w_1 and truncation distances of $d_{\max} = 10\Delta x_{\min}$ (b) and $d_{\max} = 21\Delta x_{\min}$ (c).

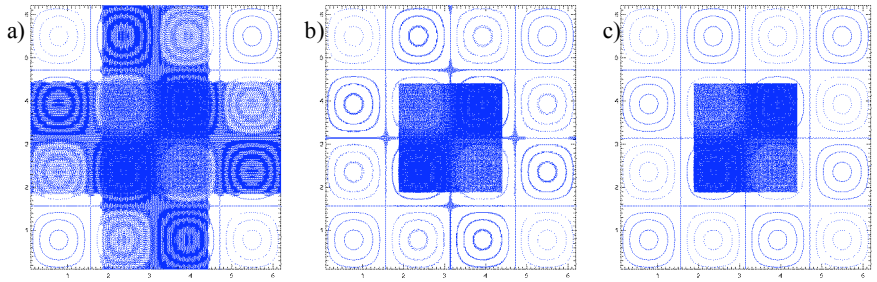

Figure 2: The initial test field on the 2D stretched-grid with $S \cong 4$ (a). The filtered fields after application of a convolution filter with 1D weighting function w_1 and truncation distances of $10\Delta x_{\min}$ (b) and $21\Delta x_{\min}$ (c).

The proposed approach appears to be a valuable alternative to a conventional grid-point based smoothing operator for stretched-grid models. The filter can be used to render quasi-isotropic fields on variable-resolution grids. A key element of this approach is that the weighting function is based on the physical distance rather than grid point indices. The convolution filter developed in 1D and generalised for 2D Cartesian geometry will next be adapted for polar geometry.

References

Surcel, D., 2005: Filtres universels pour les modèles numériques à résolution variable. Mémoire de maîtrise en Sciences de l'atmosphère, Département des Sciences de la Terre et de l'Atmosphère, Université du Québec à Montréal, 104pp.

Surcel, D., and R. Laprise, 2010: A General Filter for Stretched-Grid Models: Application in Cartesian Geometry. *Mon. Wea. Rev.* doi: 10.1175/2010MWR3531.1.

A FORMAL APPROACH FOR SMOOTHING ON VARIABLE-RESOLUTION GRID
Part II: Filtering the scalars on the polar grid

Dorina Surcel and René Laprise
ESCER, Université du Québec à Montréal, Montréal, Québec, Canada (colan@sca.uqam.ca

The filter formulation developed in 1D and generalized in 2D Cartesian domain (Surcel and Laprise 2010) is here adapted to 2D cylindrical polar geometry, as a step towards spherical polar geometry. The filter is tested for different scalar test-functions, first to control the "pole problem" specific of the latitude-longitude models, and second to remove the anisotropic noise outside the high-resolution area of a polar stretched grid.

On the polar grid the formulation of the filter is obtained by separate applications of the filter in radial and azimuthal directions. The filtered function can be written in integral form as

$$\overline{\psi}(r,\lambda) = \left(\overline{\overline{(\psi)}^{\lambda}}\right)^{r}(r,\lambda) = \int_{r'=0}^{\infty}\int_{\lambda'=0}^{2\pi}\psi(r',\lambda')\, w\left(r'(\lambda-\lambda')\right) w(r-r')\, r'\, dr'\, d\lambda' .$$

On a discrete polar grid (r_i,λ_j), the field to be filtered is represented by $\psi_{i,j} = \psi(r_i,\lambda_j)$, with $i = 1,\ldots,n; j = 1,\ldots,m$ and $r_i \in [0,R_e], \lambda_j \in [0,2\pi[$ where R_e is the distance from the centre of the grid to the boundary (henceforth referred to as the equator). Then the convolution formula is discretized as follows:

$$\overline{\psi}^{r,\lambda}(r_i,\lambda_j) = \frac{\sum_k \overline{\psi}^{\lambda}(r_k,\lambda_j)\cdot w\left(d^{r}_{i-k}\right)\cdot s(r_k)}{\sum_k w\left(d^{r}_{i-k}\right)\cdot s(r_k)} = \frac{\sum_k\sum_l \psi(r_k,\lambda_l)\cdot w\left(d^{\lambda}_{j-l}\right)\cdot w\left(d^{r}_{i-k}\right)\cdot s(r_k)\cdot s(\lambda_l)}{\sum_k\sum_l w\left(d^{\lambda}_{j-l}\right)\cdot w\left(d^{r}_{i-k}\right)\cdot s(r_k)\cdot s(\lambda_l)}$$

where d^{r}_{i-k} and d^{λ}_{j-l} are the radial and azimuthal distances, and $s(r_k)\cdot s(\lambda_l) = s(r_k,\lambda_l)$ is the unit area surface. It must be noted that the weighting function varies with the physical distances, and is not based on grid-point count, which is in fact the critical ingredient in the design of the proposed convolution filter.

To test the skill of the filter at alleviating the "pole problem", we employ a discrete uniform polar grid. The test functions are composed of a large-scale field referred to as the signal or physical component and a small-scale field referred to as the noise. The large-scale signal will be represented by a double cosine in physical space or by a cylindrical harmonic (eigenfunction of the Laplacian on the polar grid). The small-scale noise will be represented by a double cosine in physical space.

A first example regarding the application of the filter to remove the "pole problem" is presented in Fig. 1a. The test function is composed from a large-scale signal in form of a double cosine with wavelength $20{,}000\,\text{km}$ and a similar noise with wavelength of $500\,\text{km}$. The convolution filter is defined such as to keep unchanged all scales larger than $2{,}400\,\text{km}$ and to remove all scales smaller than $800\,\text{km}$. With these parameters the quadrature requires a minimum truncation distance of $1{,}600\,\text{km}$ for an adequate accuracy of the convolution. The second example presented in Fig. 1b uses a large-scale signal in form of cylindrical harmonic with radial and azimuthal wavenumbers equal to 2 and a noise with wavelength of $600\,\text{km}$. For this example the filter is designed such as to keep unchanged all scales larger than $2{,}400\,\text{km}$, but to remove all scales smaller than $1{,}000\,\text{km}$. Because the weighting function corresponds to a more abrupt response function, the convolution needs a larger truncation distance of $2{,}300\,\text{km}$ to properly remove the noise and to preserve the large-scale signal. To quantitatively assess the influence of the cut-off distance, three different weighting functions were tested. The normalized root mean square error (*NRMS*) is computed between the filtered solution and the expected analytical solution. The parameters characterizing these weighting functions are $w1(L_a = 2{,}400\,\text{km}; L_b = 1{,}000\,\text{km})$, $w2(L_a = 2{,}400\,\text{km}; L_b = 800\,\text{km})$ and $w3(L_a = 2{,}400\,\text{km}; L_b = 600\,\text{km})$, where L_a represents the minimal wavelength to be preserved and L_b the maximal wavelength to be removed by the filter. The *NRMS* curve represented in Fig.1c for truncation distance between $200\,\text{km}$ and $2{,}400\,\text{km}$ shows that the error decreases as the truncation distance increases,

although not monotonically. The oscillations are larger for $w1$ than for $w3$ due to Gibbs' phenomenon associated with the narrower response function, which necessitates wider stencil for accurate representation.

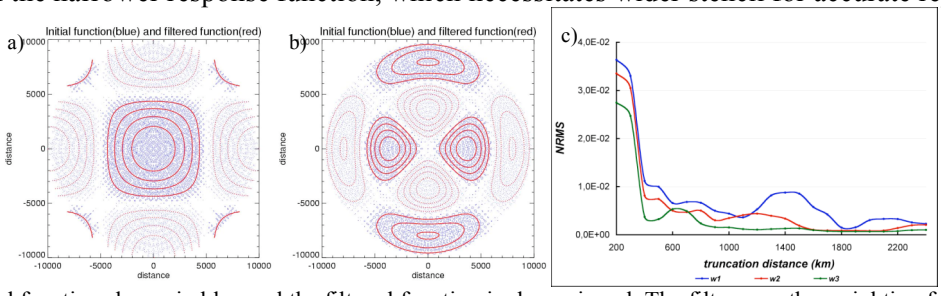

Figure 1: An initial function shown in blue and the filtered function is shown in red. The filter uses the weighting function w2 (a) and w1 (b) and truncation distances of 1,600km (a) and 2,300km (b). c) The NRMS curves as function of the truncation distance for the three weighting functions presented above.

We now present the skill of the filter at removing the anisotropy on the stretched polar grid. This grid contains a "uniform" high-resolution domain in the sector $(r_1, r_2) = (3{,}500; 7{,}500)$ km and $(\lambda_1, \lambda_2) = (5/8 \cdot 2\pi, 7/8 \cdot 2\pi)$. A gradual stretching zone is used adjacent to the high-resolution area: $r \in (2{,}500; 3{,}500) \cup (7{,}500; 8{,}500)$ and $\lambda \in (4.5/8 \cdot 2\pi, 5/8 \cdot 2\pi) \cup (7/8 \cdot 2\pi, 7.5/8 \cdot 2\pi)$, with local stretching rate of $s_r = 8\%$ in the radial direction and $s_\lambda = 3.8\%$ in the azimuthal direction. Low resolution is used elsewhere in the domain resulting in a total stretching factor of $S_r \cong S_\lambda \cong 6$.

An example of the application of the filter on the polar stretched-grid is presented in Figs 2a and 2b. The first panel represents the initial test function composed from a cylindrical harmonic with radial and azimuthal wavenumbers equal to 3 and a noise in form of a double cosine with wavelength 400km. The noise is gradually added in the stretching zones and in the high-resolution area and the filter is applied outside the uniform high-resolution region. The convolution filter uses the weighting function $w1$ and a truncation distance of 2,300km. We note that the noise is completely removed and not deformations or attenuations of the large-scale signal were observed. We verify the performance of the filter to conserve the filter quantities computing the normalized conservation ratio (*NCR*) between the initial and the filtered function. Figure 2c presents the *NCR* for a test function similar with those used for the uniform grid, but with the noise added gradually in the stretching areas and the high-resolution domain. Using the same weighting functions as in the first case we note a better conservation for weighting functions that need a smaller truncation distance, but all *NCR* curves eventually approach zero when using large truncation distances.

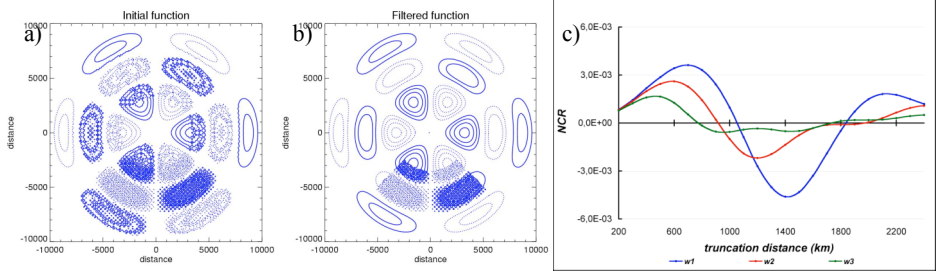

Figure 2 The initial (a) and the filtered (b) signal when the convolution filter uses the weighting function w1 and a truncation distance of 2,300km. c) The NCR curves as function of the truncation distance for the three weighting functions presented above.

The experiments realized on the polar grid demonstrated the ability of the convolution filter to adequately remove small-scale noise both in the polar region and also in the anisotropic "arms-of-the-cross" regions of the variable polar stretched grid. The convolution filter can be concomitantly applied to address the pole problem and also to remove anisotropic noise in the stretching region of the grid, by choosing appropriate parameters for the convolution weighting function.

Reference

Surcel, D., and R. Laprise, 2010: A General Filter for Stretched-Grid Models: Application in Cartesian Geometry. *Mon. Wea. Rev.* doi: 10.1175/2010MWR3531.1.

A FORMAL APPROACH FOR SMOOTHING ON VARIABLE-RESOLUTION GRID
Part III: Filtering the vectors on the polar grid

Dorina Surcel and René Laprise
ESCER, Université du Québec à Montréal, Montréal, Québec, Canada (colan@sca.uqam.ca

It is common practice to filter the fields (or sometimes their tendencies) in order to remove high wavenumbers that otherwise would affect the accuracy of a climate model. Generally, these damping methods are applied to variables such as temperature, pressure and humidity, and if filtering is needed for momentum, it is often applied to the corresponding scalar quantities, such as streamfunction and velocity potential, or vorticity and divergence. In this study we proceed to the filtering of the wind vectors themselves. The convolution filter developed by Surcel and Laprise (2010) and adapted for scalar variables on the polar grid (Surcel and Laprise 2011) is now generalized for vector fields.

When the convolution is applied to vectors such as the horizontal wind, care has to be taken to use a representation of the vector components relative to the same reference system, chosen here to correspond to the application point. As the polar grid used in this paper is an intermediate step to the application of the filter on a spherical latitude-longitude stretched grid, the representation of the vector components is made by analogy with the spherical grid.

On a polar grid defined by (r,λ), with r the radius and λ the azimuth angle, the horizontal wind is defined related to the local coordinate system, as $\mathbf{V}_h = (u, v) = \left(r\frac{d\lambda}{dt}, -\frac{dr}{dt} \right)$, where (u, v) correspond to the "zonal" and "meridional" wind components (using the terminology on the sphere), with the sign convention that u is positive eastward and v is positive northward.

The filter is applied simultaneously for both wind components and the convolution is applied successively in radial and azimuthal directions. Following the meteorological tradition, the wind components are defined relative to a locally orthogonal reference system whose base vectors change with location (only with longitude in fact for the polar grid). Therefore the application of the filter operator requires representing the wind components contributing to the convolution at a point in the same coordinate system as that point. For each point $P_0(r_i,\lambda_j)$ where the convolution filter is applied for (u,v), we transform all wind vectors in the neighbouring points $P(r_k,\lambda_l)$ contributing to the convolution, i.e. those for which their distance is within the chosen truncation distance for the convolution. The wind components at point $P(r_k,\lambda_l)$ are expressed in the coordinate system relative to the application point P_0 as follows:

$$\begin{pmatrix} u \\ v \end{pmatrix}_{P_0}(k,l) = \begin{bmatrix} \cos(\lambda_l - \lambda_j) & -\sin(\lambda_l - \lambda_j) \\ \sin(\lambda_l - \lambda_j) & \cos(\lambda_l - \lambda_j) \end{bmatrix} \begin{pmatrix} u \\ v \end{pmatrix}_{P}(k,l).$$

We note that the conversion only involves the longitude angle, not the radial distance, thus no transformation is required for points aligned on the same meridian.

To verify the efficiency of the convolution filter we define test wind fields by constructing rotational and divergent motions using the Helmholtz theorem for two-dimensional vector field $\mathbf{V}_h$ as

$$\mathbf{V}_h = \mathbf{V}_R + \mathbf{V}_D = \mathbf{k} \otimes \nabla\psi + \nabla\chi$$

where ψ is the streamfunction and χ the velocity potential. We then employ scalar test functions, for use as streamfunction or velocity potential, and we develop analytically the corresponding zonal and meridional wind components in polar coordinates. We use a signal corresponding to either a pure rotational or divergent large-scale motion, and then add to it a small-scale noise that is also either rotational or divergent.

The filter's ability for application to vectors was tested first on a uniform polar grid and we checked the performance of the filter around the pole. To verify the performance of the convolution filter we represent a large-scale wind field, considered as analytical solution, a perturbed wind field created by adding a noise to the analytic wind field, and the filtered wind field that must be identical with the analytical solution if the filter works properly.

In Fig. 1 (right panel), a streamfunction represented by a double cosine with wavelengths of 20,000 km defines a purely rotational large-scale wind field. To this large-scale field a small-scale divergent wind noise with wavelength of 500 km is added (middle panel). The convolution filter uses a weighting function that keeps unchanged all signals with wavelengths larger than 3,000km and removes all signals with wavelengths smaller than 800km. The convolution is calculated for truncation distance of 1,100 km. The filtered field (right panel) shows that the large-scale signal is preserved and the noise removed. For this test the large-scale field was located specifically such as to have not zero winds at the pole. Numerically the pole is considered as (r_1, λ_j) with $j = 1,\ldots,m$ and the convolution filter is applied there as for all other grid-points. The tests revealed that the convolution filter works properly in the vicinity of the pole, and the large-scale fields are recovered without distortions near the pole.

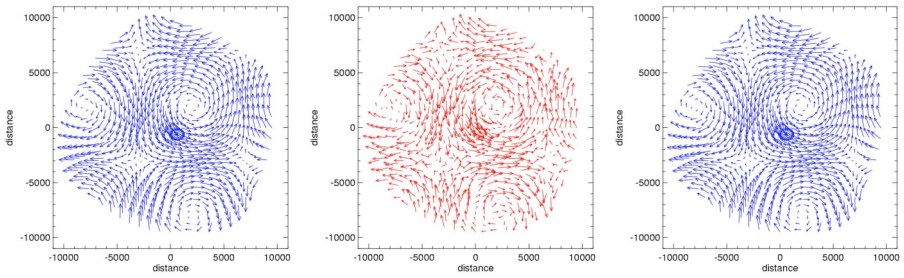

Figure 1: A large-scale rotational wind field (left panel) is perturbed by a small-scale divergent wind field (middle panel). The filtered field is represented in the right panel.

A similar experiment was repeated on a polar stretched grid. A test field wind composed from a large scale purely divergent wind developed using a velocity potential in form of cylindrical harmonic with radial wavenumber 1 and azimuthal wavenumber 2 (Fig. 2 left panel) was perturbed by a rotational noise developed using a streamfunction in form of double cosine with wavelength 400km (Fig. 2 middle panel). The filter uses a weighting function that keeps unchanged all signals with wavelengths larger than 3,000km and removes all noises with wavelengths smaller than 600km. These parameters correspond to a smoother spectral response than in the first example and thereafter necessitate a truncation distance of only 900 km to remove the noise. Because the filter is applied outside the uniform high-resolution region and to better display the effect of the filter in the stretching zones, we present only the test-function outside the high-resolution zone. In Fig.2 (right panel) we show the filtered function; visually we note that the convolution filter is able to remove the noise and after the application of the filter the large scale signal is recovered. No deformations were noted around the high-resolution domain and the filter works properly in the stretching zones as well as around the pole.

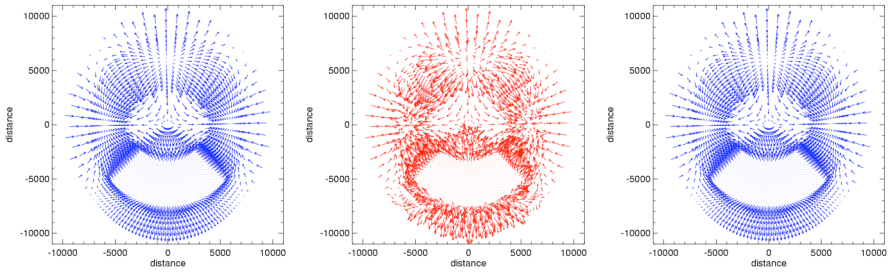

Figure 2: A large-scale divergent wind field (left panel) is perturbed by a small-scale rotational wind field (middle panel). The convolution filter is applied outside the uniform high resolution region and the filtered field is represented in the right panel.

The present study shows that with appropriate definition constraints, and representing the winds components for all points contributing to the convolution relative to the same reference system as the application point, we were able to remove small-scale noise superimposed on large-scale signals.

Reference

Surcel, D., and R. Laprise, 2010: A General Filter for Stretched-Grid Models: Application in Cartesian Geometry. *Mon. Wea. Rev.* doi: 10.1175/2010MWR3531.1.

Surcel, D., and R. Laprise, 2011: A Theoretical Approach for a Smoothing operator on a variable grid. Part II: Filtering the scalars on the polar grid, Research activities in Atmospheric and Oceanic Modelling, edited by A. Zadra, WMO/TD – No , Report No. 40.